



FIR-luminous [C II] Emitters in the ALMA-SCUBA-2 COSMOS Survey (AS2COSMOS): The Nature of Submillimeter Galaxies in a 10 Comoving Megaparsec-scale Structure at $z \sim 4.6$

I. Mitsuhashi^{1,2}, Y. Matsuda^{2,3}, Ian Smail⁴, N. H. Hayatsu^{2,5}, J. M. Simpson^{2,4,6}, A. M. Swinbank⁴, H. Umehata^{7,8},
U. Dudzevičiūtė⁴, J. E. Birkin⁴, S. Ikarashi⁴, Chian-Chou Chen⁶, K. Tadaki², H. Yajima⁹, Y. Harikane^{2,10,11}, H. Inami¹²,
S. C. Chapman¹³, B. Hatsukade⁸, D. Iono^{2,3}, A. Bunker¹⁴, Y. Ao¹⁵, T. Saito¹⁶, J. Ueda², and S. Sakamoto^{1,2}

¹Department of Astronomy, The University of Tokyo, 7-3-1 Hongo, Bunkyo, Tokyo 113-0033, Japan

²National Astronomical Observatory of Japan, 2-21-1 Osawa, Mitaka, Tokyo 181-8588, Japan

³Department of Astronomy, School of Science, SOKENDAI (The Graduate University for Advanced Studies), Osawa, Mitaka, Tokyo 181-8588, Japan

⁴Centre for Extragalactic Astronomy, Department of Physics, Durham University, Durham, DH1 3LE, UK

⁵LPENS, Ecole Normale Supérieure, Université PSL, CNRS, Sorbonne Université, Université Paris-Diderot, Paris, France

⁶Academia Sinica Institute of Astronomy and Astrophysics, No. 1, Sec. 4, Roosevelt Road, Taipei 10617, Taiwan

⁷RIKEN Cluster for Pioneering Research, 2-1 Hirosawa, Wako, Saitama 351-0198, Japan

⁸Institute of Astronomy, Graduate School of Science, The University of Tokyo, 2-21-1 Osawa, Mitaka, Tokyo 181-0015, Japan

⁹Center for Computational Physics, University of Tsukuba, Tsukuba, Ibaraki 305, Japan

¹⁰Department of Physics and Astronomy, University College London, Gower Street, London WC1E 6BT, UK

¹¹Institute for Cosmic Ray Research, The University of Tokyo, 5-1-5 Kashiwanoha, Kashiwa, Chiba 277-8582, Japan

¹²Hiroshima Astrophysical Science Center, Hiroshima University, 1-3-1 Kagamiyama, Higashi-Hiroshima, Hiroshima 739-8526, Japan

¹³Department of Physics and Atmospheric Science, Dalhousie University, Halifax, NS B3H 3J5 Canada

¹⁴Department of Physics, University of Oxford, Denys Wilkinson Building, Keble Road, OX1 3RH, UK

¹⁵Purple Mountain Observatory & Key Laboratory for Radio Astronomy, Chinese Academy of Sciences, 8 Yuanhua Road, Nanjing 210034, People's Republic of China

¹⁶Nishiharima Astronomical Observatory, Centre for Astronomy, University of Hyogo, 407-2 Nishigaichi, Sayo, Sayo-gun, 679-5313 Hyogo, Japan

Received 2020 May 16; revised 2020 October 21; accepted 2020 November 18; published 2021 February 5

Abstract

We report the discovery of a 10 comoving megaparsec (cMpc)-scale structure traced by massive submillimeter galaxies (SMGs) at $z \sim 4.6$. These galaxies are selected from an emission line search of ALMA Band 7 observations targeting 184 luminous submillimeter sources ($S_{850\mu\text{m}} \geq 6.2$ mJy) across 1.6 degrees² in the COSMOS field. We identify four [C II] emitting SMGs and two probable [C II] emitting SMG candidates at $z = 4.60\text{--}4.64$ with velocity-integrated signal-to-noise ratio of $S/N > 8$. Four of the six emitters are near-infrared blank SMGs. After excluding one SMG whose emission line is falling at the edge of the spectral window, all galaxies show clear velocity gradients along the major axes that are consistent with rotating gas disks. The estimated rotation velocities of the disks are $330\text{--}550$ km s⁻¹ and the inferred host dark-matter halo masses are $\sim 2\text{--}8 \times 10^{12} M_{\odot}$. From their estimated halo masses and [C II] luminosity function, we suggest that these galaxies have a high (50%–100%) duty cycle and high (~ 0.1) baryon conversion efficiency (SFR relative to baryon accretion rate), and that they contribute $\simeq 2\%$ to the total star formation rate density at $z = 4.6$. These SMGs are concentrated within just 0.3% of the full survey volume, suggesting they are strongly clustered. The extent of this structure and the individual halo masses suggest that these SMGs will likely evolve into members of a $\sim 10^{15} M_{\odot}$ cluster at $z = 0$. This survey reveals a synchronized dusty starburst in massive halos at $z > 4$, which could be driven by mergers or fed by smooth gas accretion.

Unified Astronomy Thesaurus concepts: Galaxy formation (595); Galaxy evolution (594); Galaxy environments (2029); High-redshift galaxy clusters (2007); Submillimeter astronomy (1647)

1. Introduction

The connection between environment and galaxy formation is likely to be critical to understanding the variety seen in the galaxy population in the local universe (Dressler 1980). Studies of the star formation activity of galaxies in overdense regions at high redshifts, which are expected to evolve into clusters by the present day, are a powerful tool to investigate the processes involved in galaxy formation (e.g., Kodama et al. 2001; Koyama et al. 2013). For example, Romano-Díaz et al. (2014) predicts that galaxies grow predominantly by smooth gas accretion from cosmological filaments in high-redshift overdense regions. Observationally testing such claims is thus a key goal of galaxy evolution studies (e.g., Umehata et al. 2019).

Submillimeter galaxies (SMGs) are dusty strongly star-forming galaxies at high redshift (e.g., Smail et al. 1997; Barger

et al. 1998; Hughes et al. 1998; Scott et al. 2010; Yun et al. 2012), which are believed to be tracers of massive dark-matter halos in the early universe (Blain et al. 1999; Hickox et al. 2012; Chen et al. 2016; Wilkinson et al. 2017; An et al. 2019; Dudzevičiūtė et al. 2020). As such, SMGs are potential signposts to identify large-scale structures (Tamura et al. 2009; Umehata et al. 2014, 2015, 2019; Casey et al. 2014; Casey 2016; Miller et al. 2018; Oteo et al. 2018; Cooke et al. 2019; Hill et al. 2020; Miller et al. 2020) and also provide insights into the formation processes of massive galaxies. The majority of SMGs are found at $z = 1\text{--}4$ and they are thought to be powered by gas-rich mergers or rapid gas accretion from the cosmic web (e.g., Tacconi et al. 2008; Umehata et al. 2019; McAlpine et al. 2019). Recently, high sensitivity interferometric observations have revealed that SMGs, including the higher-redshift examples at $z > 4$, tend to have rotating gas

disks, which may indicate that either fast gas settling in interactions, or smooth gas accretion, make an important contribution to fuel high-redshift starbursts (Hodge et al. 2012; De Breuck et al. 2014; Tadaki et al. 2018). To understand the formation process of $z > 4$ SMGs in the cosmological context, we need to study their statistical properties based on a wide-field spectroscopic survey of $z > 4$ SMGs.

The ${}^2\text{P}_{3/2}-{}^2\text{P}_{1/2}$ fine structure line of C^+ at $157.74 \mu\text{m}$ (hereafter [C II]) is one of the brightest far-infrared lines (e.g., Brauher et al. 2008; Smail et al. 2011). The [C II] line is suitable for spectroscopic identifications and studies of gas dynamics of $z > 4$ SMGs at submillimeter wavelengths (e.g., Iono et al. 2006; De Breuck et al. 2014; Jones et al. 2017). For instance, the ALMA-LABOCA Extended Chandra Deep Field-South Survey (ALESS; Hodge et al. 2013) and ALMA-SCUBA-2 survey of the UDS field (AS2UDS; Stach et al. 2019) serendipitously detected [C II] emitting SMGs at $z = 4.4\text{--}4.6$ from their ALMA Band 7 snapshot observations of large samples of submillimeter sources (Swinbank et al. 2012; Cooke et al. 2018).

In this paper, we report a search for [C II]-emitting SMGs in the Cosmic Evolution Survey (COSMOS) field, based on ALMA Band 7 snapshot observations. We take advantage of the [C II] line to investigate the star formation activity in the SMGs and the environments they reside in. Throughout this paper, we assume a Λ CDM cosmology with $\Omega_{\text{M}} = 0.3$, $\Omega_{\Lambda} = 0.7$, and $H_0 = 70 \text{ km s}^{-1} \text{ Mpc}^{-1}$.

2. Data

The targets studied in this work represent an effectively complete sample of 184 luminous ($S_{850\mu\text{m}} \geq 6.2 \text{ mJy}$) submillimeter sources across a sky area of ~ 1.64 degrees², selected from the SCUBA-2 COSMOS survey (S2COSMOS; Simpson et al. 2019). Among the 184 sources, ALMA Band 7 data of 24 sources are obtained from the ALMA data archive (2013.1.00034.S; 2015.1.00137.S; 2013.1.01292.S; 2015.1.00568.S; 2015.1.01074.S; 2016.1.01604.S; 2016.1.00478.S). We observed the remaining 160 submillimeter sources in program 2016.1.00463.S and full details of the observation, reduction, and analysis of the whole survey are presented in Simpson et al. (2020). The observations were performed with standard single continuum setup with a total bandwidth of 7.5 GHz centered on 344 GHz, split into two sidebands (335.7–339.3 GHz and 347.7–351.4 GHz), corresponding to frequency of the redshifted [C II] emission line in sources at $z = 4.40\text{--}4.46$ and $z = 4.60\text{--}4.66$, respectively. We estimate that the full survey volume for the [C II] line emission search in our study is $2.2 \times 10^6 \text{ cMpc}^3$. The FWHM of the ALMA primary beam at 344 GHz is $\sim 17''$, which covers the whole SCUBA-2 beam ($\sim 15''$). The minimum and maximum baseline lengths were 15.0 m and 313.7 m, respectively.

We calibrated the data and made dirty image cubes with Common Astronomy Software Application (CASA) version 5.6.1 (McMullin et al. 2007). The cubes have a synthesized beam of $0''.8 \times 0''.8$ and a typical 1σ depth of $\sim 2.4 \text{ mJy beam}^{-1}$ in a 27 km s^{-1} spectral channel. A more detailed description of reduction and the full catalog of the 260 continuum sources are presented in Simpson et al. (2020).

3. Analysis and Results

We search for emission lines in signal-to-noise ratio (S/N) cubes as shown in Figure 1 (see also Hayatsu et al. 2017). We start from the dirty cubes without primary beam correction, which have uniform noise levels across each field. To provide sensitivity to a wide range of line widths, we bin these data cubes to four different velocity resolutions (80, 140, 300, and 750 km s^{-1} ; see Cooke et al. 2018). To estimate the continuum level excluding emission lines, we average all channels for each spatial pixel in the binned data cubes using 2σ clipping. We iterate this procedure until the 2σ clipping converges, and subtract the resulting continuum values from the data cubes. We check that the 2σ clipped average is more stable than a linear fit without oversubtraction. We also confirm that continuum levels estimated from a median agree with those from 2σ clipped average within 10% and that the choice of the methods used in continuum estimation does not affect the following line detection. As the noise is not constant across the frequency bands, we construct the S/N cubes by dividing each channel of the binned dirty cubes by the rms of that channel measured across the full field of the cube.

In the binned, continuum-subtracted S/N cubes, we detect six line emitters with peak $S/N > 6.2$. We adopt this 6.2σ threshold on the grounds that no false detection appear in any of the inverted data cubes above this significance. This means that there is no negative peak exceeding -6.2σ in any of the 184 S/N cubes we searched. For 80, 140, 300, 750 km s^{-1} binning scales, this threshold corresponds to detection limits of [C II] luminosity of $L_{[\text{C II}]} = 0.5, 0.7, 1.1, 1.8 \times 10^9 L_{\odot}$ at $z \sim 4.5$, or observed-frame equivalent width (EW) of $\text{EW} = 0.4, 0.5, 0.8, 1.3 \mu\text{m}$ for a source with $S_{870\mu\text{m}} = 6.2 \text{ mJy}$. All of the six line emitters are associated with $870 \mu\text{m}$ continuum sources. We exclude one line emitter (AS2COS0002.1) because we cannot measure the total line flux or line velocity width of the emission line as it falls at the edge of the spectral window¹⁷ (see Figure 2). We measure the S/N of the emission lines from velocity-integrated maps between $\nu_{\text{obs}} - 0.5 \times \text{FWHM}$ and $\nu_{\text{obs}} + 0.5 \times \text{FWHM}$ at the peak pixels. Our final sample comprises five emitters with lines detected at high significance levels, integrated $S/N > 8$. We show the sky distribution of the emitters in Figure 2. All of these emitters fall within a $7'$ diameter region and a narrow frequency range (337.3–338.5 GHz).

We have checked the completeness of our line search by simulating a 1.2×10^7 Gaussian-like emission line with the range of the FWHMs of $80\text{--}2000 \text{ km s}^{-1}$ and luminosities of $10^{7.5}\text{--}10^{10.1} L_{\odot}$ and injecting them in data cubes containing a pure noise representative of the survey ($2.4 \text{ mJy beam}^{-1}$ per channel). We split FWHMs into 300 cells and luminosities into 700 cells in log space, thus there are 55 lines in each cell. From this analysis we find that the completeness is almost unity above $L_{[\text{C II}]} = 3 \times 10^9 L_{\odot}$, which is about ~ 10 times higher than the detection limits for other [C II] emitting galaxies at $z > 4$ (see Figure 3).

As the S/Ns of our detected lines are not high enough to require CLEANing, we measure the line properties using the dirty, primary-beam-corrected flux data cubes. We use the CASA/IMFIT task to measure the continuum flux densities,

¹⁷ We confirm that AS2COS0002.1 (R.A. 150.106505 deg, decl. 2.26362 deg) has a redshift of $z = 4.596$ through the detection of ${}^{12}\text{CO}(5\text{--}4)$ (C.-C. Chen et al. 2021, in preparation) and has a faint near-infrared counterpart ($K_s > 24 \text{ ABmag}$).

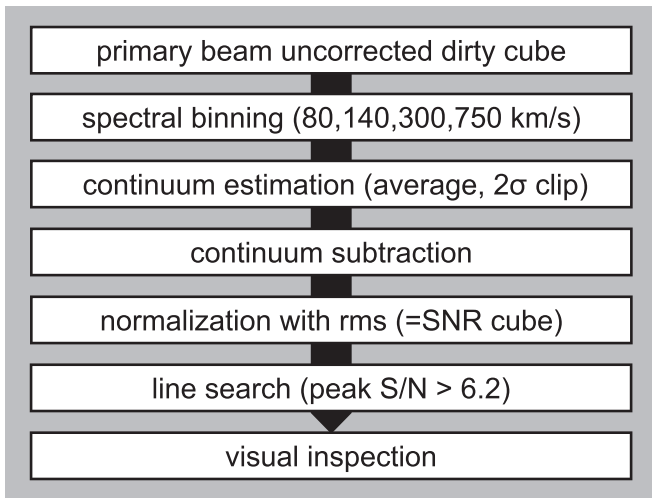


Figure 1. Flowchart of our line search method.

velocity-integrated line fluxes and sizes. The observed properties are summarized in Table 1. We recalculate continuum levels excluding channels containing the emission lines and construct line-free continuum maps. The line-free continuum maps are used to measure the spatially integrated continuum flux densities with 2D Gaussian profiles. We also construct emission line cubes by subtracting the estimated continuum values (shown as green solid lines in Figure 2) from the cubes. We measure the velocity widths of the spatially integrated emission lines using single Gaussian profiles (see Figure 2). All of the emission lines have large velocity widths: $\gtrsim 500 \text{ km s}^{-1}$. Figure 4 shows the velocity-integrated flux maps (moment 0) and the velocity maps (moment 1) of the five emitters. The spatially integrated line fluxes and beam-deconvolved major/minor axes are measured by using 2D Gaussian profiles for the line-emitting regions detected above $>3\sigma$ on the moment 0 maps. We correct for missing line flux falling into the gaps of the spectral windows by interpolating the emission lines with single Gaussian fits. The estimated missing line fluxes are $\sim 10\%$ for AS2COS0001.1, $\sim 25\%$ for AS2COS0001.2 and negligible (less than 5%) for the remaining three sources. All the five emitters show clear velocity gradients on the moment 1 maps. Since the directions of these velocity gradients match the major axis position angles, they are likely to be rotating gas disks. Simpson et al. (2020) and Jiménez-Andrade et al. (2020) have already confirmed that AS2COS0001.1/1.2 show clear rotating features with higher angular resolution ALMA data.

3.1. Line Identification

Our five line-emitting SMGs have also been detected with AzTEC on the James Clerk Maxwell Telescope (JCMT), with AS2COS0001 and AS2COS0006 corresponding to AzTEC2 and AzTEC9 (Scott et al. 2008; Younger et al. 2009). Later, AS2COS0001, AS2COS0006, and AS2COS0034 were also identified as AzTEC-C3, AzTEC-C14, and AzTEC-C30 using AzTEC on the Atacama Submillimeter Telescope Experiment (ASTE; Aretxaga et al. 2011). These SMGs are also detected in the Herschel/HerMES survey (Oliver et al. 2012) and an earlier SCUBA-2 $850 \mu\text{m}$ survey (Casey et al. 2013). While more recently, AS2COS0001.1/1.2, AS2COS0006.1, and AS2COS0034.1/34.2 were identified in ALMA Band 6 as

AzTEC-C3a/C3b, AzTEC-C14, and AzTEC-C30a/C30b (Brisbin et al. 2017).

Among the five line emitters, three have been already confirmed to be at $z \sim 4.6$. Recently, Jiménez-Andrade et al. (2020) observed the two line emitters (AS2COS0001.1/1.2) with NOthern Extended Millimeter Array (NOEMA) Band 1 and detected $^{12}\text{CO}(5-4)$ lines at $z = 4.63$ (see also Simpson et al. 2020). Birkin et al. (2021) also observed AS2COS0006.1 as a part of the large CO surveys of luminous SMGs and detected $^{12}\text{CO}(5-4)$ and [C I] at $z = 4.62$.

Their multiwavelength properties, line equivalent widths, and close proximity suggest that the remaining two sources (AS2COS0034.1/34.2) are also likely to be [C II] emitters at $z = 4.62$. Figure 5 shows multiwavelength images of the five emitters (Koekemoer et al. 2007; Sanders et al. 2007; McCracken et al. 2012; Smolčić et al. 2017). The confirmed [C II] emitters are near-infrared blank or faint SMGs ($K_s > 24$ ABmag). AS2COS0034.1/34.2 do not have any clear optical/near-infrared counterparts, which is consistent with them lying at $z \gtrsim 4$ (e.g., Simpson et al. 2014; Wang et al. 2019; Dudzevičiūtė et al. 2020; Umehata et al. 2020; Smail et al. 2020). We use the $S_{870\mu\text{m}}/S_{3\text{GHz}}$ flux ratio as a crude redshift indicator (e.g., Carilli & Yun 1999; Barger et al. 2000; Smail et al. 2000). AS2COS0034.1/34.2 have $S_{870\mu\text{m}}/S_{3\text{GHz}}$ flux ratios of 320 ± 60 and 950 ± 540 , respectively. By comparing with the typical SEDs of SMGs (Silva et al. 1998; Swinbank et al. 2010, 2014; Dudzevičiūtė et al. 2020; S. Ikarashi et al. 2021, in preparation), the flux ratios suggest that they are likely to be at $z = 3-5$ (see Figure 6). In addition, these values are consistent with those of our three confirmed [C II]-emitters at $z = 4.62-4.64$. Thus AS2COS0034.1/34.2 are unlikely to be low- or mid- J CO line emitters at $z \ll 3.0$. Moreover, the emission lines of AS2COS0034.1/34.2 have observed-frame equivalent widths of $\text{EW} = 4.5 \pm 0.8$ and $5.9 \pm 1.0 \mu\text{m}$, which are similar to the [C II] EW of the $z \sim 4.4$ SMGs (1.8 and $4.9 \mu\text{m}$) from Swinbank et al. (2012) and our three confirmed [C II]-emitters at $z = 4.62-4.64$ ($2.3-5.2 \mu\text{m}$). These observed-frame EWs are several times larger than high- J CO lines at intermediate redshifts (e.g., Hayatsu et al. 2017) and three times smaller than [O III] at $z \sim 9$ (e.g., Tamura et al. 2019). Thus AS2COS0034.1/34.2 are unlikely to be high- J CO line or [O III] emitters. Therefore we treat these two sources as [C II] emitter candidates at $z \sim 4.6$.

3.2. Gravitational Lensing

There is a $z = 0.73$ rich cluster $5'$ northeast from AS2COS0006.1 (Guzzo et al. 2007), which could amplify the emission from the SMGs either due to cluster-scale gravitational lensing (Aretxaga et al. 2011), or more realistically given the angular separation to the cluster center, by increasing the projected density of foreground galaxies, which could act as galaxy-scale lenses (e.g., Smail et al. 2005). As shown in Figure 5, there are foreground galaxies near the SMGs in the fields of AS2COS0001.1/1.2 and AS2COS0034.1/34.2, which could also amplify the emission from the SMGs by galaxy-galaxy gravitational lensing (the galaxy close to AS2COS0034.1/34.2 is indeed at $z = 0.73$). To assess the relative importance of these various lensing structures we estimate the amplification factor, μ , by using a simple singular isothermal sphere model.

The foreground $z = 0.73$ cluster has an estimated mass within R_{500} ($84''$) of $M \sim 1.7 \times 10^{14} M_{\odot}$ (Guzzo et al. 2007).

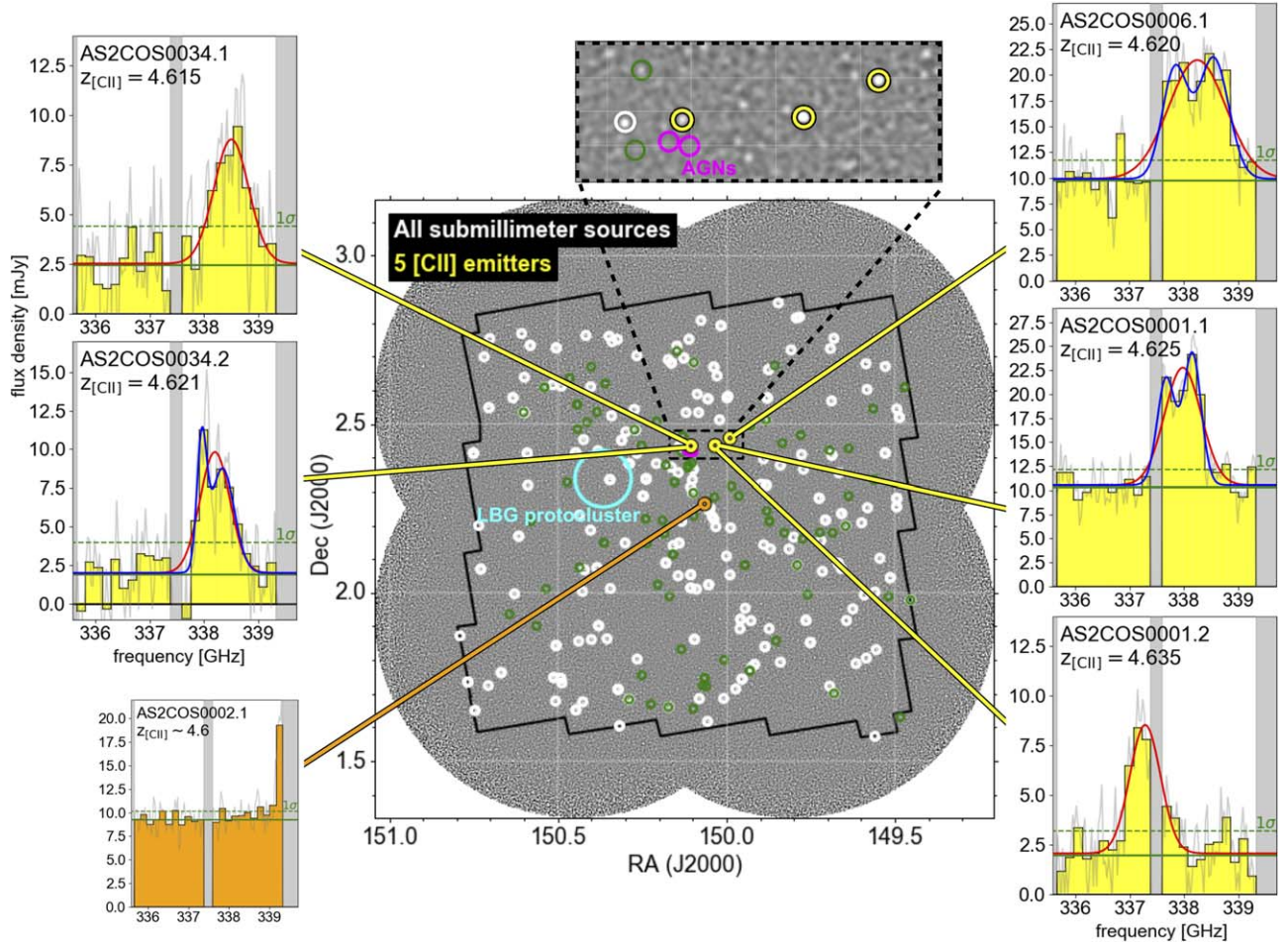


Figure 2. Sky positions of five [C II]-emitting SMGs (yellow circles) and the emitter we excluded (orange circle) with the spatially integrated spectra of their emission lines. The white circles show the positions of the parent sample of 184 SMGs from the AS2COSMOS survey (Simpson et al. 2020) and green circles show the positions of the sources from S2COSMOS and A³COSMOS (An et al. 2019; Liu et al. 2019) with photometric redshift of $z = 4-5$. The five emitters are clustered in a small sky region ($\sim 7'$ or 16 comoving Mpc) and in a narrow redshift range ($\Delta z_{[\text{C II}]}$ = 0.021 or $\Delta v = 1100 \text{ km s}^{-1}$). The background image is the $850 \mu\text{m}$ SCUBA-2 map from Simpson et al. (2019) and the black solid line shows the survey area of 1.6 degree^2 corresponding to the HST/ACS coverage. We also show two AGNs at $z = 4.64$ (Hasinger et al. 2018; magenta circles) and a protocluster at $z = 4.53-4.60$ (Lemaux et al. 2018; cyan circle). The spectra were binned to a $\sim 135 \text{ km s}^{-1}$ resolution. Red and blue lines show single and double Gaussian fits, respectively. The dashed lines show the average 1σ noise of each channel. The gray shaded regions in each spectrum show the gaps in the spectral coverage.

An isothermal model would suggest a virial velocity of $V_{\text{vir}} = 1100 \text{ km s}^{-1}$ within a virial radius of $r_{\text{vir}} = 1200 \text{ kpc}$. We extrapolate the isothermal distribution to the source separations and convert from the rotational velocity to velocity dispersion with the relationship of $\sigma^2 = V_{\text{vir}}^2/2$. The resulting predicted amplifications for AS2COS0001, AS2COS0006, and AS2COS0034 are $\mu = 1.02 \pm 0.01$, 1.04 ± 0.01 , and 1.01 ± 0.01 , which are less than 5% and negligible.

A foreground galaxy at $z = 0.33$ is located near AS2COS0001.1/1.2 (Faure et al. 2008). This galaxy has an estimated stellar mass of $M_* = 10^{11.0} M_{\odot}$ and is classified as a quiescent galaxy (Laigle et al. 2016). We convert the stellar mass to a velocity dispersion of $170 \pm 30 \text{ km s}^{-1}$ using the Faber–Jackson relation in Gallazzi et al. (2006). The predicted amplifications for AS2COS0001.1/1.2 are then $\mu = 1.4^{+0.2}_{-0.1}$ and $1.2^{+0.1}_{-0.1}$, respectively. We confirm that these amplification factors are almost comparable with the result in the previous work (Jiménez-Andrade et al. 2020; $1.5\times$ and $1.35\times$ respectively).

Similarly, a foreground galaxy at $z = 0.73$ is also located between AS2COS0034.1/34.2 (Lilly et al. 2007). We note that

different velocity peaks and different EW of the emission lines (see Figure 2 and Table 1) suggest that these two sources are not strongly lensed multiple images of a single galaxy. The foreground galaxy has an estimated stellar mass of $M_* = 10^{10.6} M_{\odot}$ and is classified as a star-forming galaxy (Laigle et al. 2016). We derive a rotation velocity of $V_{\text{rot}} = 200^{+70}_{-50} \text{ km s}^{-1}$ from the Tully–Fisher relation in Di Teodoro et al. (2016). We then convert from the rotational velocity to velocity dispersion with the relationship of $\sigma^2 = V_{\text{rot}}^2/2$. The resulting predicted amplifications for AS2COS0034.1/34.2 are $\mu = 1.1^{+0.1}_{-0.1}$ and $1.3^{+0.3}_{-0.1}$, respectively.

The influence of galaxy–galaxy lensing seems dominant for AS2COS0001.1/1.2 and AS2COS0034.1/34.2, rather than the effect of the foreground $z = 0.73$ cluster. Although we have confirmed that the expected lens amplifications due to foreground galaxies are relatively modest, we correct for these magnification factors throughout the rest of the paper.

3.3. Spatial Distribution and Environment

Figure 7 shows the 3D map of our five [C II] emitting SMGs (and candidates). We see that these SMGs are concentrated

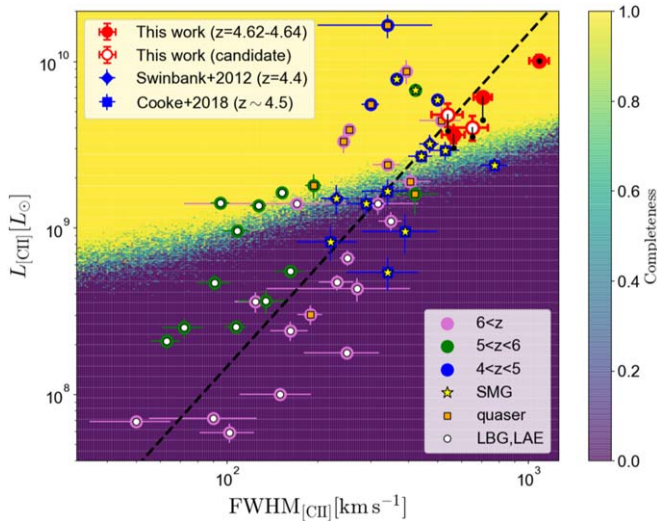


Figure 3. [C II] velocity width vs. line luminosity of the five emitters. Red and black circles show the values before and after correcting for lensing amplification (see Section 3.2). Black dashed line shows $L_{[\text{C II}]} \propto \text{FWHM}_{[\text{C II}]}$ relation scaled to the data points of SMGs. Background shows the completeness of our line search as a function of the input velocity width and input line luminosity. We confirm that the completeness is almost unity above $L_{[\text{C II}]} = 3 \times 10^9 L_{\odot}$. The literature values come from Iono et al. (2006), Wagg et al. (2010), Wang et al. (2013), Willott et al. (2013), Ouchi et al. (2013), Carniani et al. (2013, 2018), Riechers et al. (2014), Capak et al. (2015), Maiolino et al. (2015), Willott et al. (2015), Yun et al. (2015), Pentericci et al. (2016), Miller et al. (2016), Venemans et al. (2016), Smit et al. (2018), Hashimoto et al. (2019), and Harikane et al. (2020).

within a $7'.0 \times 1'.4$ region on the sky (16×3 cMpc² at $z = 4.6$) and a narrow redshift range of $\Delta z = 0.021$ (12 cMpc at $z = 4.6$), which correspond to just $\simeq 0.3\%$ of the full survey volume (gray shaded regions in Figure 7, see Section 2). The SMG distribution appears to link to the surrounding larger scale structure (see Figures 2 and 7). AS2COS0002.1 at $z = 4.596$ is located $10'$ (20 cMpc in projection) south from the SMG structure. There are two AGNs at $z = 4.64$ very close to the SMG structure (Hasinger et al. 2018). There is also a protocluster of LBGs at $z = 4.53$ – 4.60 (Lemaux et al. 2018), which is $20'$ (40 cMpc in projection) apart from the SMG structure. There are 91 SMGs with photometric redshifts of $z = 4$ – 5 from S2COSMOS and A³COSMOS (An et al. 2019; Liu et al. 2019). Some of the SMGs could be at $z = 4.6$ and are potentially related with the SMG structure. Future observations will be able to reveal their possible connections and the whole picture of the larger scale structure.

3.4. Dark Matter Halo Mass

We estimate the individual dark matter halo masses, M_h , for each of the line emitter SMGs adopting an idealized spherical collapse model (e.g., Barkana & Loeb 2001). This assumes that the galaxy’s measured rotation velocity, V_{rot} , is equal to the circular velocity of the host halo (i.e., isothermal sphere; see also Posti et al. 2019; Shimasaku & Izumi 2019) and that the halo is collapsed at the observed redshift. To derive the rotation velocity we first estimate the inclination angle of the [C II]-emitting gas disks, i , with $i = \cos^{-1} a_{\text{min}}/a_{\text{maj}}$, where a_{min} and a_{maj} are the deconvolved minor and major axes of [C II] emission, respectively (see Table 1). The major axes span 4–6 kpc. We calculate the rotation velocities from the velocity widths with the following relation, $V_{\text{rot}} = 1/\gamma \times \text{FWHM}_{[\text{C II}]} / \sin i$ ($\gamma = 2$, Kohandel et al.

2019). The range of estimated halo masses of our five SMGs is 2 – $8 \times 10^{12} M_{\odot}$ within virial radii of 70–110 kpc. Since it is not clear that the assumption of the flat rotation curve is applicable to our SMGs, we check the consistency with different methods for the halo mass calculation. The mass range of calculated halos corresponds to a bias of $b = 8.3 \pm 1.9$ at $z = 4.6$ (Mo & White 2002), which is consistent with $b = 8.4 \pm 0.7$ derived from the clustering analysis for $z = 3$ – 5 SMGs (e.g., An et al. 2019). In addition, the typical separation of our five SMGs is ~ 10 cMpc and this is comparable to the predicted clustering length of the halos with masses of $M_h \gtrsim 2 \times 10^{12} M_{\odot}$ (~ 10 cMpc; Mo & White 2002). The main uncertainties in the halo masses come from the inclination measurements of the gas disks. The $\sin i$ of AS2COS0001.1, 6.1, and 34.1 are determined with $\sim 15\%$ precision. We confirm that the measured inclination and V_{rot} of AS2COS0001.1 is consistent with those presented in the previous work with higher resolution data within 1σ uncertainties ($i = 51 \pm 3^\circ$ and $V_{\text{rot}} = 540 \pm 90 \text{ km s}^{-1}$; Jiménez-Andrade et al. 2020). We note that we can only place lower limits on the halo masses for AS2COS0001.2 and 34.2 due to the larger uncertainties of their inclination measurements. Future higher resolution and deeper observations are needed for more precise estimates.

As shown in Figures 2 and 5, our sample contains two SMG pairs, each of which could reside in common halos. We estimate their common halo masses from the sky separation and the velocity separation of these pairs assuming an NFW dark-matter profile (Table 1; Navarro et al. 1997). We use the concentration parameter of $c = 3.5$, as expected for halos of $M_h \sim 10^{12} M_{\odot}$ at $z \sim 4.5$ (Dutton & Macciò 2014). Since we ignore the line-of-sight separations and the velocities in the transverse direction, the estimated halo masses with the NFW profile are lower limits. AS2COS0001.1/1.2 have an angular separation of $3''.1$ (~ 21 kpc) and a redshift offset of $\Delta z = 0.010 \pm 0.002$ ($\Delta v = 560 \pm 50 \text{ km s}^{-1}$ or $\Delta d = 1.04 \pm 0.20$ pMpc). AS2COS0034.1/34.2 have an angular separation of $5''.0$ (~ 33 kpc) and a redshift offset of $\Delta z = 0.006 \pm 0.002$ ($\Delta v = 310 \pm 60 \text{ km s}^{-1}$ or $\Delta d = 0.52 \pm 0.20$ pMpc). The estimated lower limits are $6.4^{+2.3}_{-1.8} \times 10^{12} M_{\odot}$ for ASCOS0001 and $0.8^{+0.6}_{-0.4} \times 10^{12} M_{\odot}$ for AS2COS0034, and they are consistent with the halo masses derived from the rotation velocities of the gas disks (Figure 8(a)).

4. Discussion

4.1. Nature of High-redshift SMGs

We discuss the nature of $z > 4$ bright SMGs in a cosmological context. By comparing with predictions from a Λ CDM model, we estimate the duty cycle, baryon conversion efficiency, and contribution to the cosmic SFRD of the high-redshift SMGs with the full COSMOS survey volume of 2.2×10^6 cMpc³.

In Figure 8(a), we plot the cumulative number density of the five [C II] emitting SMGs and the $z = 4.6$ halo mass function from Angulo et al. (2012). We also show 1σ uncertainty of halo mass function comes from the cosmic variance (Mo & White 2002; Moster et al. 2011). We find that the 50%–100% halos at $z = 4.6$ with a mass of $M_h \gtrsim 4 \times 10^{12} M_{\odot}$ host SMGs. Such a high duty cycle for bright SMGs could be explained by continuous rapid gas accretion in massive, high-redshift halos or by a series of short duration starbursts

Table 1
Properties of the Five Emission-line-detected SMGs

ID ^a	AS2COS0001.1	AS2COS0001.2	AS2COS0006.1	AS2COS00034.1	AS2COS0034.2
R.A.(deg) ^a	150.03350	150.03268	149.98871	150.10446	150.10572
decl.(deg) ^a	2.43675	2.43701	2.45850	2.43537	2.43481
$\mu S_{870\mu\text{m}}$ (mJy) ^b	12.2 ± 0.4	3.2 ± 0.2	12.5 ± 0.5	4.1 ± 0.3	3.7 ± 0.2
$\mu S_{3\text{GHz}}$ (μJy) ^c	15.0 ± 2.4	28.8 ± 2.7	13.2 ± 3.3	13.0 ± 2.4	3.9 ± 2.2
ν_{obs} (GHz)	337.90	337.27	338.17	338.49	338.14
$z_{[\text{C II}]}$	4.625 ± 0.001	4.635 ± 0.001	4.620 ± 0.001	4.615 ± 0.001	4.621 ± 0.001
FWHM _[C II] (km s ⁻¹)	710 ± 50	560 ± 50	1090 ± 80	650 ± 80	540 ± 60
$Sdv_{[\text{C II}]}$ (Jy km s ⁻¹) ^d	7.0 ^{+0.8} _{-1.3}	4.7 ^{+0.6} _{-0.6}	15.9 ± 1.3	5.5 ^{+1.0} _{-1.1}	6.0 ^{+1.1} _{-1.7}
$L_{[\text{C II}]}$ (10 ⁹ L_{\odot})	4.4 ^{+0.5} _{-0.8}	3.0 ^{+0.4} _{-0.4}	10.1 ± 0.8	3.5 ^{+0.6} _{-0.7}	3.8 ^{+0.7} _{-1.1}
SFR _[C II] (M_{\odot} yr ⁻¹)	390 ⁺³⁵⁰ ₋₁₈₀	260 ⁺²⁴⁰ ₋₁₂₀	880 ⁺⁷⁹⁰ ₋₄₂₀	310 ⁺²⁸⁰ ₋₁₅₀	330 ⁺³⁰⁰ ₋₁₆₀
S/N ^e	15.3	10.0	17.4	8.0	10.7
EW(μm) ^f	2.3 ± 0.2	5.2 ± 0.7	3.7 ± 0.3	4.5 ± 0.8	5.9 ± 1.0
size _[C II] (" × ") ^g	0.6 ^{±0.1} × 0.4 ^{±0.1}	0.6 ^{±0.1} × 0.5 ^{±0.2}	0.9 ^{±0.1} × 0.2 ^{±0.1}	0.8 ^{±0.2} × 0.1 ^{±0.3}	0.6 ^{±0.3} × 0.4 ^{±0.3}
i (deg)	47 ± 9	34 ⁺²⁸ ₋₃₄	77 ± 8	80 ⁺¹⁰ ₋₂₁	52 ⁺³⁴ ₋₅₂
V_{rot} (km s ⁻¹)	470 ± 80	490 ⁻¹⁸⁰ ^h	550 ± 40	330 ⁺⁵⁰ ₋₁₀	340 ⁻⁷⁰ ^h
M_h^{ind} (10 ¹² M_{\odot})	5.1 ± 1.4	5.7 ^{-3.6} ^h	8.0 ± 1.1	1.7 ^{+0.4} _{-0.1}	1.9 ^{-0.7} ^h
M_h^{NFW} (10 ¹² M_{\odot}) ⁱ		6.4 ^{+2.3} _{-1.8}	...		0.8 ^{+0.6} _{-0.4}
M_{dyn} (10 ¹¹ M_{\odot})	1.7 ± 0.3	1.9 ^{-0.9} ^h	2.3 ± 0.3	0.8 ^{+0.2} _{-0.1}	0.9 ^{-0.3} ^h
SFR _{870μm} (M_{\odot} yr ⁻¹) ^j	390 ⁺⁸⁰ ₋₁₀	230 ⁺³⁰ ₋₁₀	450 ⁺¹⁰ ₋₁₀	260 ⁺³⁰ ₋₁₀	240 ⁺⁴⁰ ₋₁₀
μ ^k	1.4 ^{+0.2} _{-0.1}	1.2 ^{+0.1} _{-0.1}	...	1.1 ^{+0.1} _{-0.1}	1.3 ^{+0.3} _{-0.1}

Notes.

^a Source IDs and coordinates come from the full AS2COSMOS catalog presented in Simpson et al. (2020).

^b Total continuum flux densities excluding line emission measured with the CASA/IMFIT task.

^c Radio continuum fluxes from Smolčić et al. (2017).

^d Total emission line flux measured with the CASA/IMFIT task.

^e Velocity-integrated peak emission line S/N within the FWHM.

^f Observed-frame line equivalent widths.

^g Beam-deconvolved major and minor axes measured with the CASA/IMFIT task.

^h Upper limits cannot be constrained from uncertainty of the inclinations.

ⁱ Common halo masses assuming NFW dark matter profile.

^j Star formation rate estimated from $S_{870\mu\text{m}}$ and conversion in Dudzevičiūtė et al. (2020).

^k Gravitational magnification factors.

triggered via galaxy interactions. We note that the latter interpretation is more consistent with the fact that several of the SMGs may share common halos, where the proximity of the neighboring sources would then also explain the triggering of the intense star formation within these systems. McAlpine et al. (2019) predict that mergers are a necessary, but not sufficient, condition to create an SMG: a massive gas reservoir is also needed to power the intense star formation activity. Therefore a combination of triggering by near-continuous mergers and/or rapid gas fueling by gas accretion might be necessary to produce bright high-redshift bright SMGs with such high duty cycles.

Owing to the large survey volume of AS2COSMOS, we constrain the $z \sim 4.6$ [C II] luminosity function brighter than $L_{[\text{C II}]} > 3 \times 10^9 L_{\odot}$ (Figure 8(b)). Above this luminosity, we have confirmed that completeness correction due to our line search is not necessary for our constraints (see Section 3). Here, we calculate the number densities for two cases, one for the full sample of the five SMGs, and one with the subset of two SMGs with $S_{870\mu\text{m}} \geq 6.2$ mJy. As our continuum survey is complete to the level of 6.2 mJy, the number density of the full sample of five SMGs gives only a lower limit due to the missing fainter-continuum [C II] emitters in our survey volume. We note that if AS2COS0034.1/34.2 are not [C II] emitters, then the number density corresponding to our quoted lower limit should be reduced to 40% (2/5). With the previous results from

Swinbank et al. (2012) and Cooke et al. (2018) we find that the bright end of the [C II] luminosity function gradually decrease toward $L_{[\text{C II}]} \sim 10^{10} L_{\odot}$.

We compare the [C II] luminosity function with model luminosity functions derived from the halo mass function. McBride et al. (2009) predicts that the mean baryon accretion rate (\dot{M}) into a halo as a function of virial mass M_{vir} and redshift z is given by the following equation,

$$\langle \dot{M} \rangle = f_{\text{baryon}} \times 42 \left(\frac{M_{\text{vir}}}{10^{12} M_{\odot}} \right)^{1.127} \times (1 + 1.17z) \sqrt{\Omega_{\text{M}}(1+z)^3 + \Omega_{\Lambda}}, \quad (1)$$

where f_{baryon} is the baryon-to-dark matter ratio of $\sim 1/6$. The difference of $\langle \dot{M} \rangle$ in the corresponding halo mass range is less than 20% across the literature (McBride et al. 2009; Dekel et al. 2009; Goerdt et al. 2015). We convert the halo masses to the baryon accretion rates with Equation (1), and calculate SFRs assuming that accreted gas becomes stars with baryon conversion efficiencies of $\epsilon = 0.01, 0.1, 1.0$. This baryon conversion efficiency is defined as SFR divided by baryon accretion rate (see Behroozi et al. 2013, 2019). With the SFRs, we calculate $L_{[\text{C II}]}$ from the following relation in De Looze

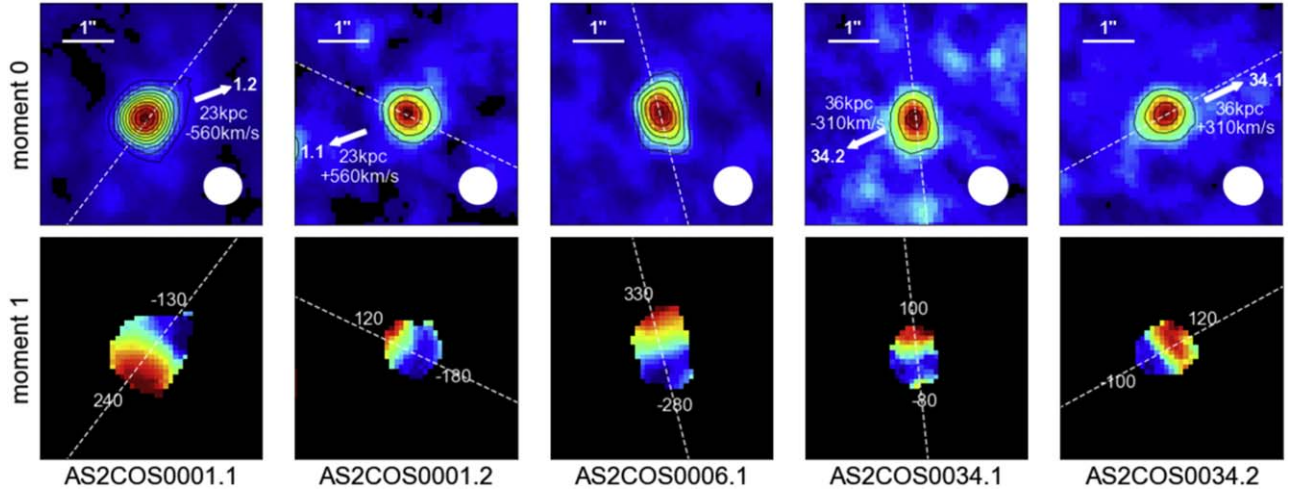


Figure 4. Top: the velocity-integrated flux maps of five detected line-emitting SMGs. The black contours show the surface brightness of the emission lines starting from 3σ with 2σ intervals. Velocity offsets, projected spatial separations, and directions of any companions (if they have one) are also shown. The dashed lines show major-axis position angles. Bottom: the velocity maps with 3σ clipping. Typical velocities (in km s^{-1}) and major axis position angles are also denoted. All of the five sources show clear velocity gradients along the major axes that are consistent with rotating disks.

et al. (2014).

$$\log \text{SFR} = -7.06 + 1.00 \times \log L_{[\text{C II}]} \quad (2)$$

We note that this conversion includes a 1σ dispersion of 0.27 dex (shaded areas in Figure 8(b)). We find that the model luminosity function with a baryon conversion efficiency of $\epsilon \sim 0.1$ agrees well with the observed luminosity function at least at the bright end (where our survey is likely complete). The inferred baryon conversion efficiency of $\epsilon \sim 0.1$ is similar to that estimated for normal star-forming galaxies with halo masses of $M_h \sim 10^{12} M_\odot$, although at lower redshifts $z \sim 2$ (Behroozi et al. 2013), which could also have a high duty cycle of $>50\%$ (Daddi et al. 2005) and have been claimed to be fed by smooth gas accretion (Dekel et al. 2009). The halos with a mass of $M_h \gtrsim 4 \times 10^{12} M_\odot$ at $z = 4.6$ are expected to have a smooth gas accretion rate of $\gtrsim 800 M_\odot \text{ yr}^{-1}$, which is about half of the total baryon accretion rate (Goerdt et al. 2015). Thus the gas accretion for such halos could be sufficient to achieve the high SFR seen in the SMGs. Of course this does not rule out gas accretion through mergers especially given that four of our five targets are potentially close pairs.

We estimate the contribution of the bright SMGs at $z = 4.6$ to the cosmic star formation rate density (SFRD). The contribution of dust-obscured galaxies to the cosmic SFRD is less well constrained at $z > 4$ (e.g., Madau & Dickinson 2014; Swinbank et al. 2014; Casey et al. 2018; Zavala et al. 2018; Dudzevičiūtė et al. 2020). The number density and luminosity of [C II] emitters provide robust lower limits on the SFRD at this epoch. We calculate the SFRD of SMGs based on the two bright SMGs for which our survey is complete above its flux level of $S_{870\mu\text{m}} \geq 6.2 \text{ mJy}$ across the survey volume (Figure 9). We convert [C II] luminosities to SFR with Equation (2). Here, the error is dominated by the uncertainties from the $L_{[\text{C II}]}$ -SFR conversion. We confirm that the [C II]-based SFRs are consistent with those derived from the dust continuum assuming the relation in Dudzevičiūtė et al. (2020).

The contribution of the bright continuum-detected SMGs to the total SFRD is $\simeq 2\%$ at $z = 4.6$. This is comparable with the contribution of dust continuum-selected SMGs presented in

previous works when we use the same flux cutoff ($S_{870\mu\text{m}} \geq 6.2 \text{ mJy}$; Cooke et al. 2018; Dudzevičiūtė et al. 2020). In contrast, Zavala et al. (2018) claimed that the contribution of dust-obscured galaxies at $z > 4$ is $\sim 35\%$ – 85% based on an ALMA 3 mm survey. The apparent lower contribution of the bright SMGs may come from our high flux cutoff. The flux cutoff of $S_{870\mu\text{m}} \geq 6.2 \text{ mJy}$ corresponds to $\text{SFR} = 330 M_\odot \text{ yr}^{-1}$ (Dudzevičiūtė et al. 2020), which is ~ 4 times higher than the flux limit in Zavala et al. (2018; assuming a modified blackbody with $T_d = 35 \text{ K}$ and $\beta = 1.8$). In addition, as extensively discussed by Zavala et al. (2018), their sample may also be biased due to the survey including sources associated with the primary targets in the archival fields or due to synchrotron contributions to their 3 mm fluxes. We find that the cosmic SFRD can be reproduced when we integrate our model of [C II] luminosity function with $\epsilon \sim 0.1$ down to $L_{[\text{C II}]} = 10^{7.5} L_\odot$ and convert the [C II] luminosity density to SFRD using the Equation (2). This indicates that we need at least ~ 100 times deeper observations to place a meaningful constraint to the cosmic SFRD from the [C II] luminosity function.

4.2. SMG Large-scale Structure and the Descendant

The rough alignment of the five SMGs apparent in Figure 2 may suggest that simultaneous star formation activity is occurring in massive halos along the cosmic web. Numerical simulations predict that more than 90% of dark matter is in the form of unvirialized filamentary large-scale structure at $z \sim 5$ (Haider et al. 2016).

The scale of the SMG-traced structure is comparable with expected size of protoclusters at $z = 4.6$ (Chiang et al. 2013). Numerical simulations suggest that most halos with a mass of $M_h \gtrsim 2 \times 10^{12} M_\odot$ at $z = 4.6$ evolve into a $M_h \gtrsim 10^{15} M_\odot$ halo by $z = 0$ (e.g., Zhao et al. 2009), which corresponds to the present day's most massive cluster. As shown in Figure 8(a), the expected number of $M_h \sim 10^{15} M_\odot$ halos is about unity in our survey volume at $z = 0$. The present-day $\sim 10^{15} M_\odot$ halos are expected to have a maximum baryon conversion efficiency of $\epsilon \sim 0.1$ at $z \sim 4$ – 7 (Behroozi et al. 2013), which is consistent with our findings (see Section 4.1). We suggest,

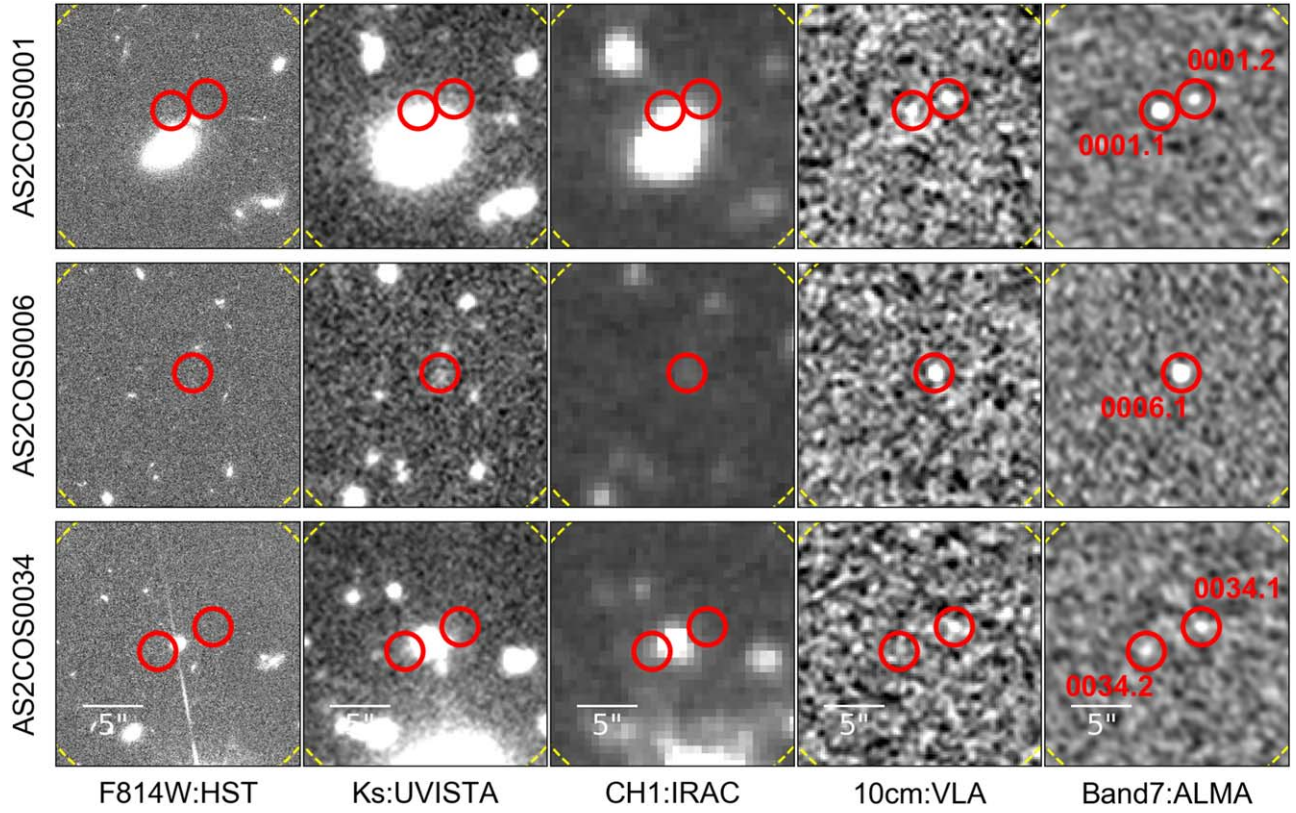


Figure 5. Multiwavelength images of the five line-emitting SMGs. The small red circles show the positions of ALMA Band 7 continuum sources (Table 1). The yellow dashed circles indicate the ALMA field of view. AS2COS0034.1/34.2 do not have detected counterparts in the optical or near-infrared bands (similar to AS2COS0001.1/1.2), suggesting that they are also likely to be at $z > 4$. In the fields of AS2COS0001 and AS2COS0034, there are foreground galaxies near the SMGs, which could modestly magnify the sources due to gravitational lensing (see Section 3.2).

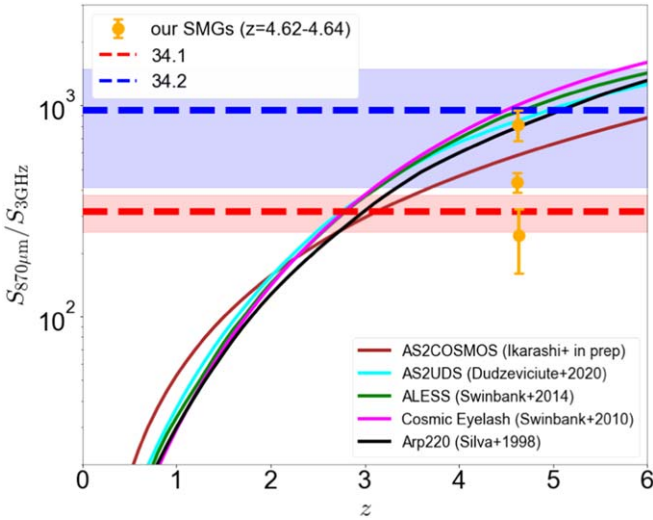


Figure 6. The $S_{870\mu\text{m}}/S_{3\text{GHz}}$ flux ratio as a function of redshift. The colored curves show the predicted ratios based on the SEDs of Arp220, Cosmic Eyelash, and various composite SMGs (Silva et al. 1998; Swinbank et al. 2010, 2014; Dudzevičiūtė et al. 2020, S. Ikarashi et al. 2021, in preparation). The flux ratios of AS2COS0034.1/34.2 suggest that they are likely to lie at $z = 3\text{--}5$ and are comparable with the ratios of the confirmed [C II]-selected SMGs at $z = 4.62\text{--}4.64$.

therefore, that we are witnessing efficient, synchronized star formation in massive galaxies, driven by mergers and potentially smooth gas accretion, within a massive protocluster environment at $z \sim 4.6$ when the universe was only 10% of its current age.

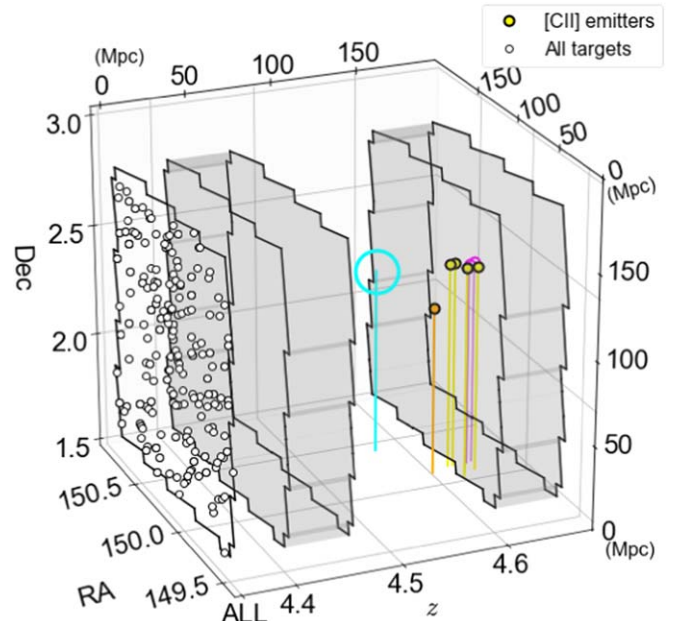


Figure 7. 3D map of [C II] emitters (and candidates) in the full survey volume. Symbols are as in Figure 2. We see that the [C II] emitters are both spatially concentrated on the sky (as shown in Figure 2), but also in 3D space.

5. Summary

We detected emission lines from six SMGs based on ALMA S2COSMOS Band 7 observations of 184 luminous submillimeter sources with $S_{850\mu\text{m}} \geq 6.2$ mJy in the full 1.6 deg^2

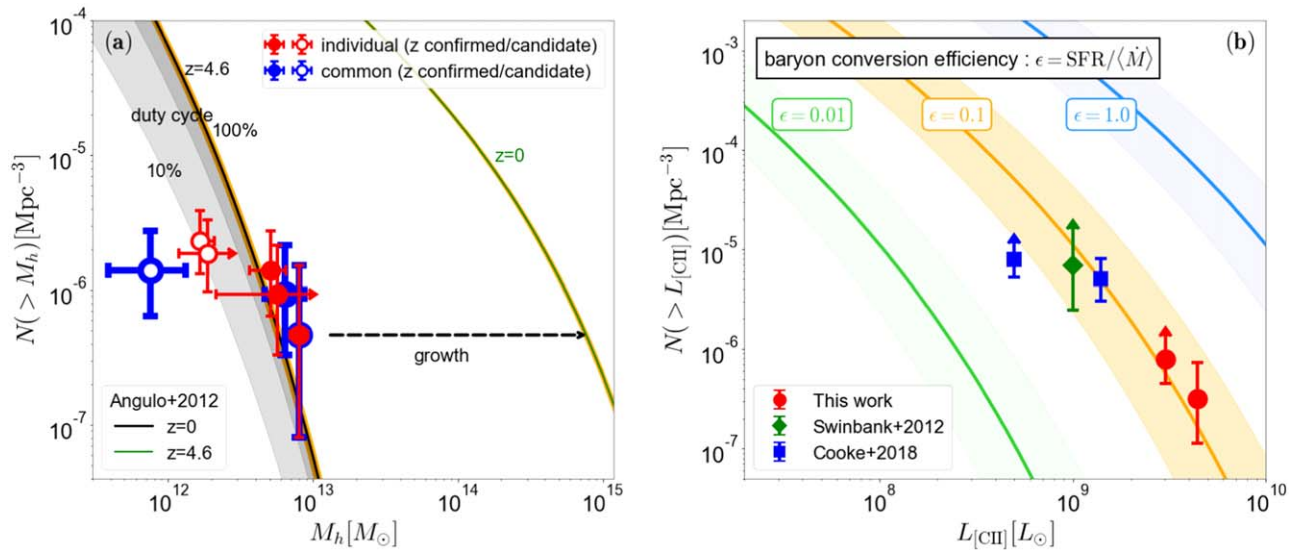


Figure 8. (a) Cumulative number density of dark matter halos for the three [C II] emitting SMGs (filled circles) at $z = 4.6$ and two candidates (open circles) calculated using a survey volume of $2.2 \times 10^6 \text{ cMpc}^3$. We plot two cases: where the five SMGs reside in individual halos (red) and where two SMG pairs share common halos (blue). The black and green curves show the halo mass functions at $z = 4.6$ and $z = 0$ predicted from a Λ CDM model (Angulo et al. 2012) with 1σ uncertainties assuming cosmic variance (orange shades; Mo & White 2002; Moster et al. 2011). The gray areas show 50%–100% and 10%–50% of the number densities. We find that the 50%–100% halos with $M_h \geq 4 \times 10^{12} M_\odot$ host SMGs at $z = 4.6$. In the same survey volume, the expected number of $\sim 10^{15} M_\odot$ halos is about unity at $z = 0$. (b) The [C II] cumulative number densities derived from five SMGs and two bright ($S_{870\mu\text{m}} \geq 6.2 \text{ mJy}$) SMGs in the COSMOS survey area. The value from five SMGs is only a lower limit due to the fact that these are also continuum-selected sources. We show the previous observational constraints at $z \sim 4.5$ (Swinbank et al. 2012; Cooke et al. 2018). Our result constrains the bright end of the luminosity function at $z = 4.6$. From the comparison with the model luminosity functions (see the text), our constraints imply a baryon conversion efficiency (defined as SFR divided by baryon accretion rate) of $\epsilon \sim 0.1$ at least for the most luminous source.

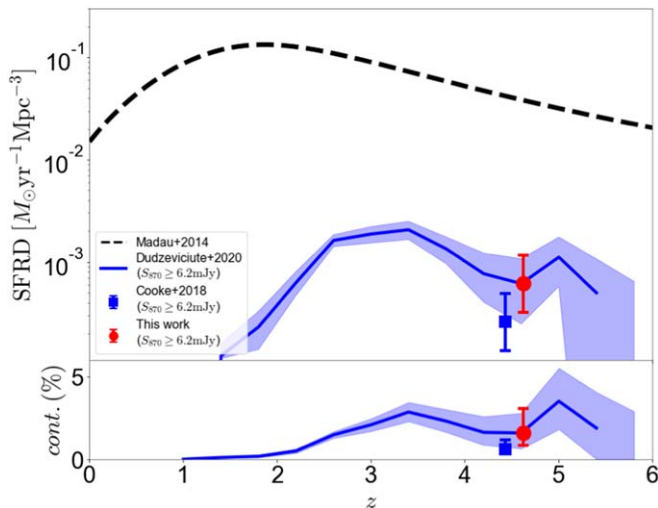






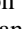









Figure 9. Cosmic star formation rate density (SFRD; Madau & Dickinson 2014) and the contribution from bright ($S_{870\mu\text{m}} \geq 6.2 \text{ mJy}$) SMGs. The red filled circle shows the SFRD derived from the two brightest SMGs in this survey (AS2COS0001.1/6.1). The blue square and curve show the previous observational constraints from $z \sim 4.5$ [C II] emitting SMGs and $z = 1$ – 6 SMGs with $S_{870\mu\text{m}} \geq 6.2 \text{ mJy}$ (Cooke et al. 2018; Dudzevičiūtė et al. 2020). We estimate that the contribution of bright continuum-detected SMGs to the cosmic star formation rate density is $\simeq 2\%$ at $z = 4.6$.

COSMOS field (Simpson et al. 2020). Among these, four SMGs have been confirmed to be [C II]($157.74 \mu\text{m}$) emitters at $z = 4.60$ – 4.64 by independent detections of $^{12}\text{CO}(J = 5$ – $4)$ emission. The remaining two SMGs are also likely to be [C II] emitters at $z = 4.62$ from their line equivalent widths and multiwavelength spectral energy distributions. Four of the six SMGs are near-infrared blank SMGs. After excluding one SMG whose emission line is falling at the edge of spectral window, all line-emitting SMGs show clear velocity gradients

along the major axes of their [C II] emission, consistent with gas disks with rotation velocities of 330 – 550 km s^{-1} . We estimate that they have individual dark matter halo masses of 2 – $8 \times 10^{12} M_\odot$, a 50%–100% duty cycle, and a baryon conversion efficiency (SFR relative to baryon accretion rate) of $\epsilon \sim 0.1$ and contribute $\simeq 2\%$ to the total SFRD at this redshift. Five SMGs are concentrated within a $16 \times 4 \times 12 \text{ cMpc}^3$ region and likely evolve into members of a massive ($\sim 10^{15} M_\odot$) cluster at $z \sim 0$. Our work demonstrates that the combination of wide-field single dish survey and ALMA follow-up is a powerful method to investigate the rapid formation process of massive galaxies within the cosmic web at $z > 4$.

We would like to thank the anonymous referee for a thoughtful and constructive report, which improved the content and clarity of this paper. We also thank to C. Casey, H. Nagai, and T. Michiyama for the useful discussion and information. Y. M., H.U., and H.I. acknowledge support from JSPS KAKENHI Grants (17H04831, 17KK0098, 19H00697, 17K14252, 20H01953, and 19K23462). I.R.S., J.M.S., U.D., A.M.S., and J.E.B. acknowledge support from STFC(ST/T000244/1). C.C. C. acknowledges support from the Ministry of Science and Technology of Taiwan (MOST 109-2112-M-001-016-MY3). This paper makes use of the following ALMA data: ADS/JAO.ALMA #2013.1.00034.S, #2015.1.00137.S, #2015.1.00568.S, #2015.1.01074.S, #2016.1.01604.S, #2016.1.00478.S, and #2016.1.00463.S. ALMA is a partnership of ESO (representing its member states), NSF (USA) and NINS (Japan), together with NRC (Canada) and NSC and ASIAA (Taiwan), in cooperation with the Republic of Chile. The Joint ALMA Observatory is operated by ESO, AUI/NRAO, and NAOJ. Data analyses were carried out on the common use data analysis computer system at ADC/NAOJ.

ORCID iDs

I. Mitsuhashi  <https://orcid.org/0000-0001-7300-9450>
 Y. Matsuda  <https://orcid.org/0000-0003-1747-2891>
 Ian Smail  <https://orcid.org/0000-0003-3037-257X>
 N. H. Hayatsu  <https://orcid.org/0000-0003-2112-1306>
 J. M. Simpson  <https://orcid.org/0000-0002-8521-1995>
 A. M. Swinbank  <https://orcid.org/0000-0003-1192-5837>
 H. Umehata  <https://orcid.org/0000-0003-1937-0573>
 Chian-Chou Chen  <https://orcid.org/0000-0002-3805-0789>
 K. Tadaki  <https://orcid.org/0000-0001-9728-8909>
 Y. Harikane  <https://orcid.org/0000-0002-6047-430X>
 H. Inami  <https://orcid.org/0000-0003-4268-0393>
 B. Hatsukade  <https://orcid.org/0000-0001-6469-8725>
 D. Iono  <https://orcid.org/0000-0002-2364-0823>
 Y. Ao  <https://orcid.org/0000-0003-3139-2724>

References

- An, F. X., Simpson, J. M., Smail, I., et al. 2019, *ApJ*, 886, 48
 Angulo, R. E., Springel, V., White, S. D. M., et al. 2012, *MNRAS*, 426, 2046
 Aretxaga, I., Wilson, G. W., Aguilar, E., et al. 2011, *MNRAS*, 415, 3831
 Barger, A. J., Cowie, L. L., & Richards, E. A. 2000, *AJ*, 119, 2092
 Barger, A. J., Cowie, L. L., Sanders, D. B., et al. 1998, *Natur*, 394, 248
 Barkana, R., & Loeb, A. 2001, *PhR*, 349, 125
 Behroozi, P., Wechsler, R. H., Hearin, A. P., & Conroy, C. 2019, *MNRAS*, 488, 3143
 Behroozi, P. S., Wechsler, R. H., & Conroy, C. 2013, *ApJ*, 770, 57
 Birkin, J. E., Weiss, A., Wardlow, J. L., et al. 2021, *MNRAS*, 501, 3926
 Blain, A. W., Smail, I., Ivison, R. J., & Kneib, J. P. 1999, *MNRAS*, 302, 632
 Brauher, J. R., Dale, D. A., & Helou, G. 2008, *ApJS*, 178, 280
 Brisbin, D., Miettinen, O., Aravena, M., et al. 2017, *A&A*, 608, A15
 Capak, P. L., Carilli, C., Jones, G., et al. 2015, *Natur*, 522, 455
 Carilli, C. L., & Yun, M. S. 1999, *ApJL*, 513, L13
 Carniani, S., Maiolino, R., Smit, R., & Amorin, R. 2018, *ApJL*, 854, L7
 Carniani, S., Marconi, A., Biggs, A., et al. 2013, *A&A*, 559, A29
 Casey, C. M. 2016, *ApJ*, 824, 36
 Casey, C. M., Chen, C.-C., Cowie, L. L., et al. 2013, *MNRAS*, 436, 1919
 Casey, C. M., Narayanan, D., & Cooray, A. 2014, *PhR*, 541, 45
 Casey, C. M., Zavala, J. A., Spilker, J., et al. 2018, *ApJ*, 862, 77
 Chen, C.-C., Smail, I., Ivison, R. J., et al. 2016, *ApJ*, 820, 82
 Chiang, Y.-K., Overzier, R., & Gebhardt, K. 2013, *ApJ*, 779, 127
 Cooke, E. A., Smail, I., Stach, S. M., et al. 2019, *MNRAS*, 486, 3047
 Cooke, E. A., Smail, I., Swinbank, A. M., et al. 2018, *ApJ*, 861, 100
 Daddi, E., Dickinson, M., Chary, R., et al. 2005, *ApJL*, 631, L13
 De Breuck, C., Williams, R. J., Swinbank, M., et al. 2014, *A&A*, 565, A59
 De Looze, I., Cormier, D., Leboutteiller, V., et al. 2014, *A&A*, 568, A62
 Dekel, A., Birnboim, Y., Engel, G., et al. 2009, *Natur*, 457, 451
 Di Teodoro, E. M., Fraternali, F., & Miller, S. H. 2016, *A&A*, 594, A77
 Dressler, A. 1980, *ApJ*, 236, 351
 Dudzevičiūtė, U., Smail, I., Swinbank, A. M., et al. 2020, *MNRAS*, 494, 3828
 Dutton, A. A., & Macciò, A. V. 2014, *MNRAS*, 441, 3359
 Faure, C., Kneib, J.-P., Covone, G., et al. 2008, *ApJS*, 176, 19
 Gallazzi, A., Charlot, S., Brinchmann, J., & White, S. D. M. 2006, *MNRAS*, 370, 1106
 Goerdt, T., Ceverino, D., Dekel, A., & Teyssier, R. 2015, *MNRAS*, 454, 637
 Guzzo, L., Cassata, P., Finoguenov, A., et al. 2007, *ApJS*, 172, 254
 Haider, M., Steinhauser, D., Vogelsberger, M., et al. 2016, *MNRAS*, 457, 3024
 Harikane, Y., Ouchi, M., Inoue, A. K., et al. 2020, *ApJ*, 896, 93
 Hashimoto, T., Inoue, A. K., Mawatari, K., et al. 2019, *PASJ*, 71, 71
 Hasinger, G., Capak, P., Salvato, M., et al. 2018, *ApJ*, 858, 77
 Hayatsu, N. H., Matsuda, Y., Umehata, H., et al. 2017, *PASJ*, 69, 45
 Hickox, R. C., Wardlow, J. L., Smail, I., et al. 2012, *MNRAS*, 421, 284
 Hill, R., Chapman, S., Scott, D., et al. 2020, *MNRAS*, 495, 3124
 Hodge, J. A., Carilli, C. L., Walter, F., et al. 2012, *ApJ*, 760, 11
 Hodge, J. A., Karim, A., Smail, I., et al. 2013, *ApJ*, 768, 91
 Hughes, D. H., Serjeant, S., Dunlop, J., et al. 1998, *Natur*, 394, 241
 Iono, D., Yun, M. S., Elvis, M., et al. 2006, *ApJL*, 645, L97
 Jiménez-Andrade, E. F., Zavala, J. A., Magnelli, B., et al. 2020, *ApJ*, 890, 171
 Jones, G. C., Carilli, C. L., Shao, Y., et al. 2017, *ApJ*, 850, 180
 Kodama, T., Smail, I., Nakata, F., Okamura, S., & Bower, R. G. 2001, *ApJL*, 562, L9
 Koekemoer, A. M., Aussel, H., Calzetti, D., et al. 2007, *ApJS*, 172, 196
 Kohandel, M., Pallottini, A., Ferrara, A., et al. 2019, *MNRAS*, 487, 3007
 Koyama, Y., Smail, I., Kurk, J., et al. 2013, *MNRAS*, 434, 423
 Laigle, C., McCracken, H. J., Ilbert, O., et al. 2016, *ApJS*, 224, 24
 Lemaux, B. C., Le Fèvre, O., Cucciati, O., et al. 2018, *A&A*, 615, A77
 Lilly, S. J., Le Fèvre, O., Renzini, A., et al. 2007, *ApJS*, 172, 70
 Liu, D., Lang, P., Magnelli, B., et al. 2019, *ApJS*, 244, 40
 Madau, P., & Dickinson, M. 2014, *ARA&A*, 52, 415
 Maiolino, R., Carniani, S., Fontana, A., et al. 2015, *MNRAS*, 452, 54
 McAlpine, S., Smail, I., Bower, R. G., et al. 2019, *MNRAS*, 488, 2440
 McBride, J., Fakhouri, O., & Ma, C.-P. 2009, *MNRAS*, 398, 1858
 McCracken, H. J., Milvang-Jensen, B., Dunlop, J., et al. 2012, *A&A*, 544, A156
 McMullin, J. P., Waters, B., Schiebel, D., Young, W., & Golap, K. 2007, in *ASP Conf. Ser.*, 376, CASA Architecture and Applications, ed. R. A. Shaw, F. Hill, & D. J. Bell (San Francisco, CA: ASP), 127
 Miller, T. B., Chapman, S. C., Aravena, M., et al. 2018, *Natur*, 556, 469
 Miller, T. B., Chapman, S. C., Hayward, C. C., et al. 2020, *ApJ*, 889, 98
 Mo, H. J., & White, S. D. M. 2002, *MNRAS*, 336, 112
 Moster, B. P., Somerville, R. S., Newman, J. A., & Rix, H.-W. 2011, *ApJ*, 731, 113
 Navarro, J. F., Frenk, C. S., & White, S. D. M. 1997, *ApJ*, 490, 493
 Oliver, S. J., Bock, J., Altieri, B., et al. 2012, *MNRAS*, 424, 1614
 Oteo, I., Ivison, R. J., Dunne, L., et al. 2018, *ApJ*, 856, 72
 Ouchi, M., Ellis, R., Ono, Y., et al. 2013, *ApJ*, 778, 102
 Pentericci, L., Carniani, S., Castellano, M., et al. 2016, *ApJL*, 829, L11
 Posti, L., Fraternali, F., & Marasco, A. 2019, *A&A*, 626, A56
 Riechers, D. A., Carilli, C. L., Capak, P. L., et al. 2014, *ApJ*, 796, 84
 Romano-Díaz, E., Shlosman, I., Choi, J.-H., & Sadoun, R. 2014, *ApJL*, 790, L32
 Sanders, D. B., Salvato, M., Aussel, H., et al. 2007, *ApJS*, 172, 86
 Scott, K. S., Austermann, J. E., Perera, T. A., et al. 2008, *MNRAS*, 385, 2225
 Scott, K. S., Yun, M. S., Wilson, G. W., et al. 2010, *MNRAS*, 405, 2260
 Shimasaku, K., & Izumi, T. 2019, *ApJL*, 872, L29
 Silva, L., Granato, G. L., Bressan, A., & Danese, L. 1998, *ApJ*, 509, 103
 Simpson, J. M., Smail, I., Dudzevičiūtė, U., et al. 2020, *MNRAS*, 495, 3409
 Simpson, J. M., Smail, I., Swinbank, A. M., et al. 2019, *ApJ*, 880, 43
 Simpson, J. M., Swinbank, A. M., Smail, I., et al. 2014, *ApJ*, 788, 125
 Smail, I., Dudzevičiūtė, U., Stach, S. M., et al. 2020, *arXiv:2010.02250*
 Smail, I., Ivison, R. J., & Blain, A. W. 1997, *ApJL*, 490, L5
 Smail, I., Ivison, R. J., Owen, F. N., Blain, A. W., & Kneib, J. P. 2000, *ApJ*, 528, 612
 Smail, I., Smith, G. P., & Ivison, R. J. 2005, *ApJ*, 631, 121
 Smail, I., Swinbank, A. M., Ivison, R. J., & Ibar, E. 2011, *MNRAS*, 414, L95
 Smit, R., Bouwens, R. J., Carniani, S., et al. 2018, *Natur*, 553, 178
 Smolčić, V., Novak, M., Bondi, M., et al. 2017, *A&A*, 602, A1
 Stach, S. M., Dudzevičiūtė, U., Smail, I., et al. 2019, *MNRAS*, 487, 4648
 Swinbank, A. M., Karim, A., Smail, I., et al. 2012, *MNRAS*, 427, 1066
 Swinbank, A. M., Simpson, J. M., Smail, I., et al. 2014, *MNRAS*, 438, 1267
 Swinbank, A. M., Smail, I., Longmore, S., et al. 2010, *Natur*, 464, 733
 Tacconi, L. J., Genzel, R., Smail, I., et al. 2008, *ApJ*, 680, 246
 Tadaki, K., Iono, D., Yun, M. S., et al. 2018, *Natur*, 560, 613
 Tamura, Y., Kohno, K., Nakanishi, K., et al. 2009, *Natur*, 459, 61
 Tamura, Y., Mawatari, K., Hashimoto, T., et al. 2019, *ApJ*, 874, 27
 Umehata, H., Fumagalli, M., Smail, I., et al. 2019, *Sci*, 366, 97
 Umehata, H., Smail, I., Swinbank, A. M., et al. 2020, *A&A*, 640, L8
 Umehata, H., Tamura, Y., Kohno, K., et al. 2014, *MNRAS*, 440, 3462
 Umehata, H., Tamura, Y., Kohno, K., et al. 2015, *ApJL*, 815, L8
 Venemans, B. P., Walter, F., Zschaechner, L., et al. 2016, *ApJ*, 816, 37
 Wagg, J., Carilli, C. L., Wilner, D. J., et al. 2010, *A&A*, 519, L1
 Wang, R., Wagg, J., Carilli, C. L., et al. 2013, *ApJ*, 773, 44
 Wang, T., Schreiber, C., Elbaz, D., et al. 2019, *Natur*, 572, 211
 Wilkinson, A., Almaini, O., Chen, C.-C., et al. 2017, *MNRAS*, 464, 1380
 Willott, C. J., Carilli, C. L., Wagg, J., & Wang, R. 2015, *ApJ*, 807, 180
 Willott, C. J., Omont, A., & Bergeron, J. 2013, *ApJ*, 770, 13
 Younger, J. D., Fazio, G. G., Huang, J.-S., et al. 2009, *ApJ*, 704, 803
 Yun, M. S., Aretxaga, I., Gurwell, M. A., et al. 2015, *MNRAS*, 454, 3485
 Yun, M. S., Scott, K. S., Guo, Y., et al. 2012, *MNRAS*, 420, 957
 Zavala, J. A., Casey, C. M., da Cunha, E., et al. 2018, *ApJ*, 869, 71
 Zhao, D. H., Jing, Y. P., Mo, H. J., & Börner, G. 2009, *ApJ*, 707, 354